Hindawi
International Journal of Energy Research
Volume 2023, Article ID 8207527, 18 pages
https://doi.org/10.1155/2023/8207527

Research Article

Numerical Simulations for Lithium-Ion Battery Pack Cooled by Different Minichannel Cold Plate Arrangements

Yulong Li,[1] Minli Bai,[1] Zhifu Zhou,[2] Wei-Tao Wu,[3] Linsong Gao,[1] Yang Li,[1] Yunjie Yang,[1] Yubai Li,[1] and Yongchen Song[1]

[1]*Key Laboratory of Ocean Energy Utilization and Energy Conservation of Ministry of Education, Dalian University of Technology, Dalian 116023, China*
[2]*State Key Laboratory of Multiphase Flow in Power Engineering, Xi'an Jiaotong University, Xi'an 710049, China*
[3]*School of Mechanical Engineering, Nanjing University of Science and Technology, Nanjing 210094, China*

Correspondence should be addressed to Yubai Li; liyubai2021@126.com and Yongchen Song; songyc@dlut.edu.cn

Received 15 October 2022; Revised 8 December 2022; Accepted 12 January 2023; Published 10 February 2023

Academic Editor: Mohammadmahdi Abdollahzadehsangroudi

In real electric vehicles, the arrangement of liquid-cooled plates not only influences the thermal performance of the battery pack but also relates to the energy consumption of the BTMS and the compactness of the whole battery pack. In this study, design A, design B, design C, and design D, a total of four different arrangement designs of battery thermal management based on liquid-cooled plates with microchannels, are proposed for a 35 V battery pack composed of 12 $LiFePO_4$ pouch battery cells connected in series, and the corresponding three-dimensional electrical-thermal-fluid model is established for numerical study. The cooling effects of the four designs are discussed and compared in terms of discharge rate, contact thermal resistance, and external short circuit. For design D, cold plates are placed in front of each battery cell. The results show that design D achieves the best cooling effect with the lowest power consumption compared to the other three designs under 0.5C, 1.0C, and 2.0C discharge rate. Its maximum temperature is about 30°C, and maximum temperature difference is under 5°C. The reduction in contact thermal resistance has different effects and magnitudes for different designs with different cold plate arrangements, but the overall effect is small. In the extreme condition of external short circuit, for design D, increasing the mass flow rate can reduce the maximum temperature of design D from 76.6°C by 27.5% to 55.5°C and the temperature difference from 35.0°C by 23.4% to 26.8°C. Selecting the proper coolant flow rate can keep the maximum temperature and temperature gradient on the battery pack of design D within tolerable level, and increasing the flow rate helps to enhance the cooling effect. For the other three designs, the maximum temperatures and temperature gradients exceeded 90°C and 40°C under the external short circuit condition, and increasing the flow rate has very little effect on the performance enhancement.

1. Introduction

Stimulated by the relevant policies of many countries, electric vehicles powered by lithium-ion batteries have entered a phase of rapid development around the world [1]. Compared with traditional Ni-MH and Ni-Cr batteries, lithium-ion batteries have significant advantages in terms of energy density [2, 3], specific energy [4, 5] cycle life [6], and so on. In addition, it has a fairly low self-discharge rate [7]. Currently, as a power unit, lithium-ion batteries are widely used in electric vehicles.

However, lithium-ion batteries are more sensitive to operating temperature and storage temperature, and it has a narrow optimal operating temperature range of 15 to 35°C [8]. In general, an operating temperature between -20 and 60°C is acceptable for lithium-ion batteries [9]. Too high or too low operating temperatures can have negative effects on the performance of lithium-ion batteries. On the one hand, under low-temperature condition, the viscosity of the electrolyte will increase, which will reduce the migration rate of chemical ions in the Li-ion battery and lead to an increase in the internal resistance of the battery. On the

other hand, the increase in charge-transfer resistance at low-temperatures will greatly affect the kinetics in batteries. These two factors can lead to the degradation of Li-ion battery performance at low-temperature condition [10]. Aris and Shabani [11] conducted charge/discharge experiments on lithium-ion batteries at low-temperatures, and the results showed that the maximum battery SOC (state of charge) decreased by 7%, 12%, and 23% of the maximum initial SOC at -5°C, -10°C, and -15°C, respectively. Zhang et al. [12] investigated the degradation of lithium-ion batteries cycling under low-temperature condition study. They found that the battery DC resistance increased, and the battery capacity decreased significantly after cycling at low-temperature of -10°C. Under high-temperature condition, lithium-ion batteries are subject to aging faster, with reduced performance and lifetime. Rodrigues et al. [13] showed that at high-temperatures, the SEI (solid-electrolyte interface) in lithium-ion batteries is affected by intensified side reactions, and this process is coupled with gas evolution and changes of SEI composition that consume active lithium ions, leading to irreversible decay of battery capacity. Gabrisch et al. [14] investigated the capacity changes of the lithium-ion batteries with LiCoO2 and LiMn2O4 as cathode materials after aging at 75°C for 10 and 6 days, respectively, and the results showed a significant decrease in battery capacity for both cathode materials. They concluded by X-ray diffractometry that the high-temperature led to the crystallographic transformation and the irreversible insertion of lithium ions into the cathode lattices, which resulted in the loss of cathode capacity. Bandhauer et al. [15] concluded based on numerous studies that when the operating temperature of lithium-ion batteries is higher than 50°C, a decrease in battery capacity occurs in all cases. In addition, under high-temperature conditions, the rate of exothermic reactions in lithium-ion batteries will be accelerated, which will release more heat and cause a further increase in battery temperature, which may eventually lead to uncontrolled exothermic reactions and thermal runaway [16]. Some studies have shown that when the temperature of lithium-ion batteries exceeds 80°C, it may trigger thermal runaway and lead to battery combustion, explosion [17], and even the production of toxic gases [18]. In addition to high and low-temperatures, temperature uniformity is also an important factor that affects battery performance. In a battery pack, the temperature distribution in the battery pack is not uniform during charging and discharging due to the inconsistency of heat production within each cell, the different locations of the battery pack, and the differences of external conditions. This can lead to an electrical imbalance in the battery module and cause a degradation in the overall performance of the battery pack. To ensure the performance of the battery pack, its maximum temperature difference should be kept within 5°C [19, 20].

Electric vehicles usually require a battery thermal management system (BTMS) to maintain the operating temperature of the lithium-ion battery pack within a suitable range. Currently, commonly used BTMS are mainly based on air-cooled, liquid-cooled, and phase-change materials. Liquid-cooled BTMS has a higher heat transfer coefficient, and its cooling efficiency is higher. However, liquid-cooled systems are also usually more complex and can have leakage problems. In addition, liquid-cooled systems also tend to be accompanied by higher power consumption. The PCM-based approach is a new type of battery thermal management solution. It can effectively control the battery pack temperature in the optimal operating temperature range and ensure excellent temperature uniformity. However, it also has the problems of poor structural strength, leakage of melting material, and low thermal conductivity [21]. The liquid cooling method is the most widely used BTMS method nowadays. Depending on whether the battery pack is in direct contact with the coolant or not, the liquid cooling systems can be divided into two modes: direct contact and indirect contact. Compared with indirect contact BTMS, the cooling performance of direct contact BTMS is slightly better, but indirect contact BTMS is more suitable for practical applications [22]. The cold plate is the most common form of indirect liquid cooling, and the structure and arrangement of the liquid cooling plate are important factors affecting the performance of indirect liquid cooling BTMS [23]. Many related studies have been conducted to improve the cooling performance of the whole system by optimizing the flow channel and structural design of the liquid-cooled plate [24].

Qian et al. [25] proposed an indirect liquid cooling method based on minichannel liquid cooling plate for a prismatic lithium-ion battery pack and explored the effects of the number of channels, inlet mass flow rate, flow direction, and channel width on the thermal performance of this lithium-ion battery pack using numerical simulation method. Their results showed that the minichannel cold plate thermal management system could control the temperature of the battery pack well under 5C discharge conditions. By further improvement, the maximum temperature and maximum temperature difference of the battery pack were reduced by 13.3% and 43.3%, respectively. Zhao et al. [26] simulated and investigated the thermal behavior of a battery module consisting of 71 18650 lithium-ion battery cells under indirect liquid cooling based on channels. Wang et al. [23] investigated the effect of different cooling structures, a number of microchannel, and inlet mass flow rate on the cooling performance of the system using the maximum temperature and maximum temperature difference as criteria and derived the optimal combination of these factors through orthogonal analysis and comprehensive analysis. The optimization strategies they proposed are very instructive for the design of indirect liquid cooling systems.

In addition to temperature control, BTMS also has the role on preventing the propagation of thermal runaway in the battery pack. Zhang et al. [27] proposed a hybrid BTMS based on PCM and liquid cooling. In the case of thermal runaway, the PCM material acts as a thermal buffer, its latent heat of phase change can accommodate the huge heat generated by the lithium-ion battery in a short period during thermal runaway, and then the liquid cooling system dissipates the heat to the outer environment. In this way, the propagation of thermal runaway is prevented. Many factors

trigger thermal runaway, and both internal and external short circuits can trigger it [28]. Li et al. [29] investigated the thermal performance of a 50 V prismatic lithium-ion battery pack with a minichannel cold plate cooling system through simulation. They found that when the coolant flow rate was large enough, the maximum temperature and temperature uniformity of the pack could be controlled at an acceptable level even under 5C rapid discharge and external short circuit condition.

Due to the high sensitivity of lithium-ion batteries to temperature, it is important to analyze the thermal behavior inside the single battery and the battery pack when conducting studies related to BTMS. There are two main research tools available, experimental and numerical simulation. The numerical simulation method can match well with reality by modifying the corresponding parameters in the numerical models, and it can describe the thermal behavior inside the battery or the pack, which is impossible for experiment. Therefore, despite the slight bias, numerical simulation is still widely used in the study of BTMS [30]. The first step in conducting a numerical simulation study is to build a battery thermal model to simulate the thermal behavior of the battery. In the existing studies, battery thermal models are mainly divided into two categories. One type adds a volume thermal source term to the battery domain directly based on the principle of battery heat production as well as experimental data to simulate only the battery thermal behavior [31, 32]. The other type is to use a coupled battery model and thermal model to establish a corresponding electrochemical-thermal model, which can simulate both the electrical and thermal behavior of the battery. The main battery models used to simulate the electrical behavior are electrochemical models based on the physics of lithium-ion batteries and equivalent circuit model (ECM). The electrochemical model can accurately describe the migration behavior of lithium ions during the charging and discharging process of lithium-ion batteries. Based on porous electrode theory and concentrated solution theory, Newman's team developed the widely used pseudo-two-dimensional (P2D) model [33, 34]. Unlike the complex electrochemical model based on physics, the ECM model simulates the electrical behavior of a battery through an equivalent circuit composed of several simple electronic components, including voltage sources, resistors, and capacitors. Compared to the electrochemical model, the ECM model requires much fewer parameters [35]. Several ECM models have been proposed and applied in research [36]. Thevenin model is one of them that has been widely used. It is based on Thevenin's theorem and consists of a voltage source, a series resistor that simulates the internal resistance of the battery, and several resistor-capacitor pairs that are used to describe the dynamic response of the battery [37]. The higher the number of resistor-capacitor pairs, the higher the accuracy of the model. However, at the same time, it increases the model's complexity. To save computational costs, some BTMS studies based on the battery module scale use ECM models [38, 39].

Most existing studies on microchannel cold plates have focused on optimizing the structure, number, flow direction, and flow rate of the flow channels. There has been little discussion on the arrangement of the cold plate. In real electric vehicles, the arrangement of liquid-cooled plates not only influences the thermal performance of the battery pack but also relates to the energy consumption of the BTMS and the compactness of the whole battery pack. In this work, four designs with different arrangements of microchannel cold plates are proposed for a battery pack consisting of 12 pouch $LiFePO_4$ batteries. A multiscale electrical-thermal-fluid model is established. The three-dimensional thermal simulations are conducted based on the numerical model, and the advantages and disadvantages of the four designs are quantitatively compared by data. The cooling effects of the four designs are discussed and compared in terms of discharge rate, contact thermal resistance, and external short circuit. First, the temperature rising and temperature gradient of the four designs are investigated under different discharge rate conditions. Second, the influence of the contact thermal resistance between adjacent cells in the battery pack on the cooling effect of the four designs is investigated. Finally, the thermal performance of the four designs is compared under external short circuit condition. This study will provide a reference for the selection and design of BTMS for electric vehicles.

2. Modeling Method

2.1. Geometry Models of the Battery Pack and Cold Plates. The battery studied in this work is $LiFeO_4$/graphite pouch battery with a nominal voltage of 3.1 V and a nominal capacity of 20 Ah. Each battery cell is divided into three domains, the battery cell domain, the positive tab domain, and the negative tab domain. The geometry of the battery cell is 205.5 mm × 156 mm × 7.1 mm. The tab domains are 45 mm × 43.5 mm × 3.1 mm. The distance between the two tabs is 34 mm. The battery pack in this work is composed of 12 lithium-ion batteries connected in series by busbars whose nominal voltage is 35 V. To simulate the contact thermal resistance between adjacent cells or between the cell and the cold plate, solid contact layers with a thickness of 0.6 mm are added between every two cells or between the battery and the cold plate.

Four different arrangements of microchannel cold plate are proposed in the present work, as shown in Figure 1 (where the cyan parts represent the battery cell; the orange parts are the negative tabs; the yellow parts are the positive tabs; the gray parts on the tabs are the busbars; the black parts between the cells or between the cells and the cold plates are the contact layers; the translucent black parts are the cold plates, and the blue parts are the channels. The coordinate directions are established in the figure to convenience the analysis and discussion). Design A, design B, and design C arrange the cold plates on the front, side, and bottom of the battery pack, respectively. Each cold plate contains three minichannels. For design D, a cold plate is placed in front of each battery cell, and each cold plate contains three *n*-shaped microflow channels, with all microchannel inlet liquid coming from one main inlet and all outlet liquids converging to one main outlet. In design A, design B, and

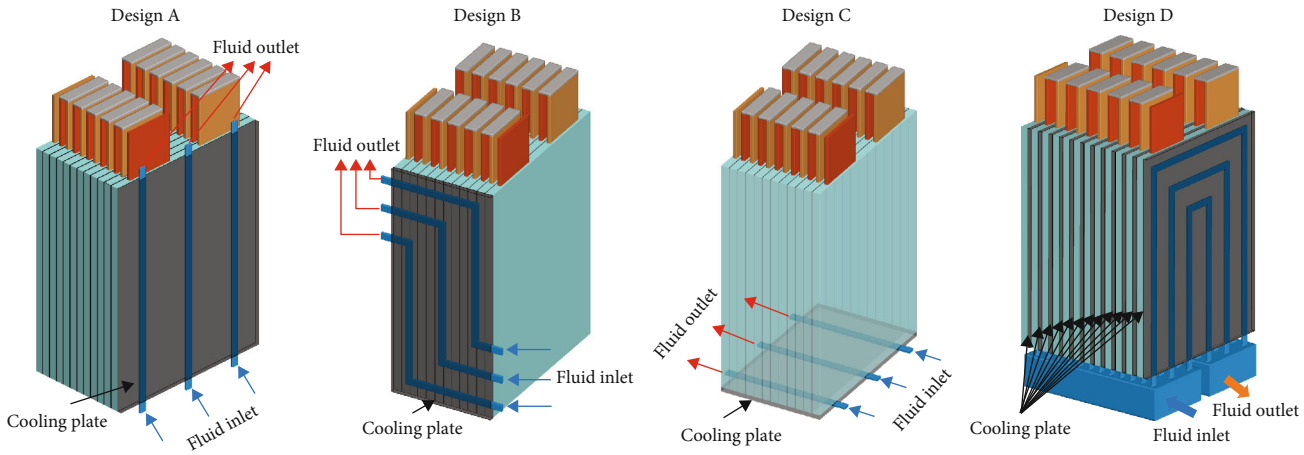

Figure 1: The geometric model of the four battery packs. (Design A: cold plate is placed on the front of the pack. Design B: cold plate is placed on the side of the pack. Design C: cold plate is placed under the pack. Design D: a cold plate is placed in front of each cell).

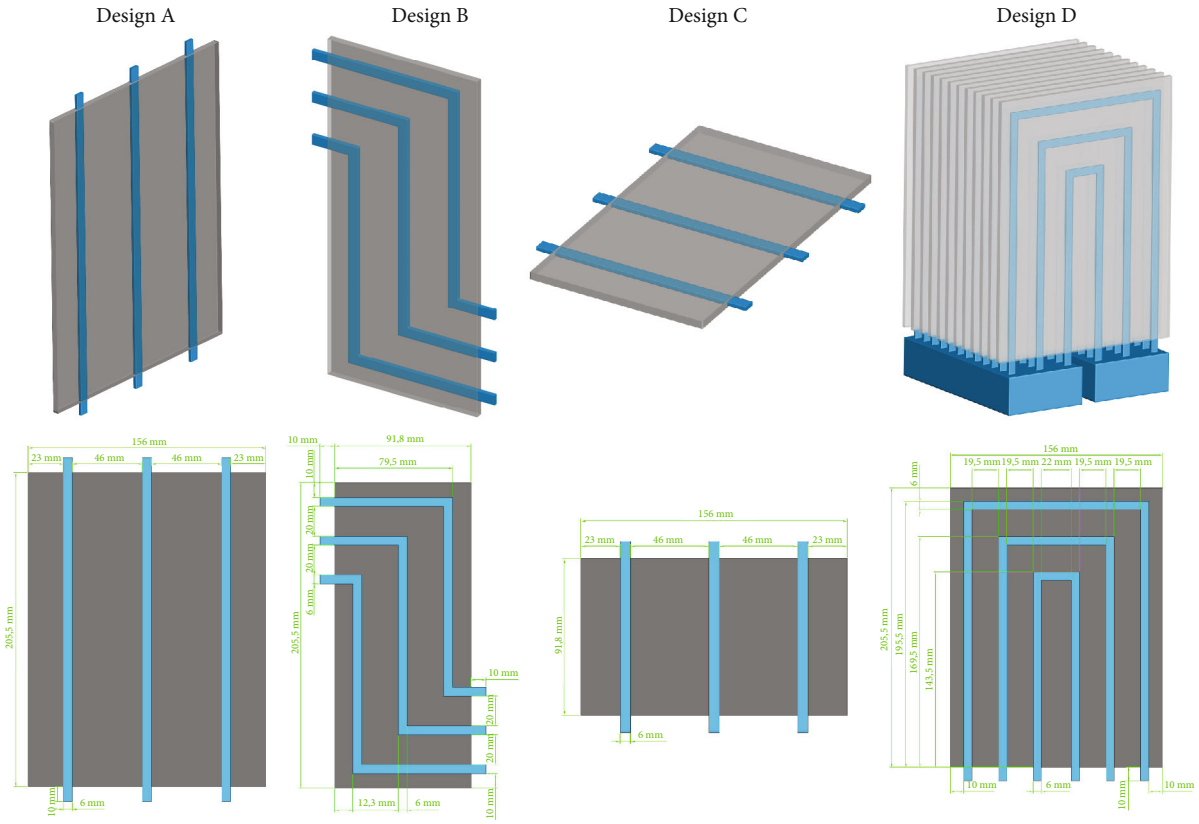

Figure 2: Geometry parameters of the cold plates in the four designs.

design C, there are three uniformly distributed microchannels in the cold plate with rectangular cross-sections for a better cooling effect. For design D, each cold plate contains three N-shaped microchannels whose cross-section shape is rectangular. The main inlet and outlet are also rectangular. The detailed geometries of these cold plates are shown in Figure 2, where the fluid zone is shown in blue and the solid zone is in gray.

To carry out numerical simulation, it is necessary to obtain the materials used in each calculation domain. In this study, water with high specific heat and low viscosity is selected as the coolant. Aluminum with low density and good thermal conductivity is chosen as the material for the cold plate. The positive tab material of the battery is aluminum, and the negative tab material is copper. In the pouch battery, the battery cell is made of several layers of cathode, separator, and anode, and the electrolyte is filled between the cathode and anode layers, as shown in Figure 3(a). Due to the layered structure of the battery cell, its thermal conductivity varies greatly in different directions. In this work,

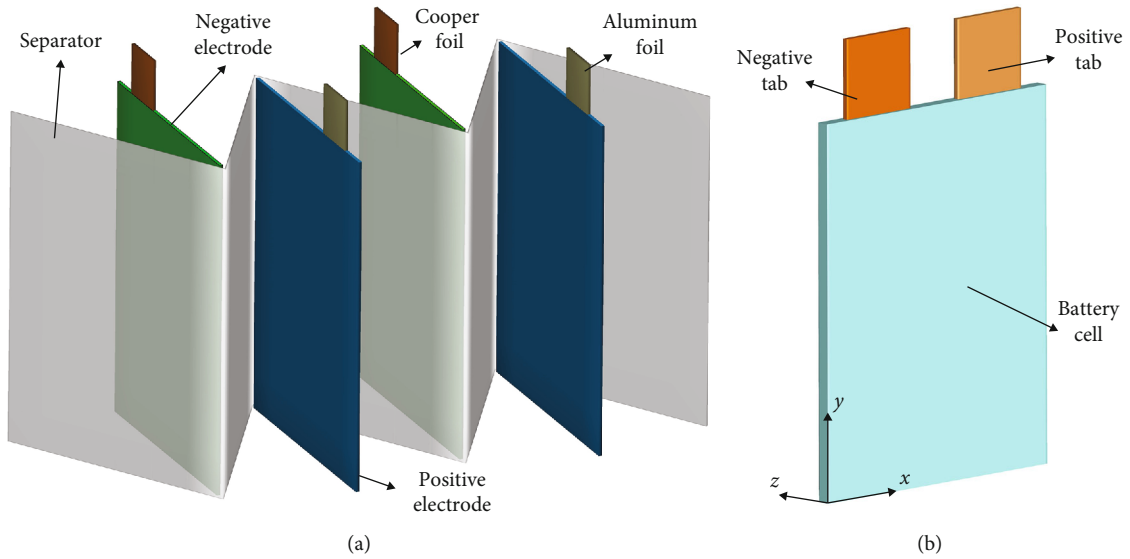

Figure 3: (a) Multilayer structure inside the pouch battery. (b) Geometric model of single battery.

Table 1: Thermal properties used in simulation.

Material	ρ (kg m^{-3})	c_p (J kg^{-1} K^{-1})	k (W m^{-1} K^{-1})	μ (kg m^{-1} s^{-1})
Battery	2115.45	1450	—	—
Aluminum	2719	871	202.4	—
Cooper	8978	381	387.6	—
Contact layer	1.225	1006.43	—	—
Water	998.2	4182	0.6	0.001003

anisotropic thermal conductivity is used for the battery cell domain. According to the calculation method of thermal conductivity of the battery cell proposed by Taheri and Bahrami [40], the thermal conductivity of the battery cell in each direction is obtained as follows:

$$\lambda_z = 0.97\text{W/(mK)}, \lambda_x = \lambda_y = 26.57\text{W/(mK)}, \quad (1)$$

where the subscripts x, y, and z refer to the directions shown in Figure 3(b).

Between two solid surfaces in contact, the actual contact occurs only on some discrete area elements, and the uncontacted place between surfaces is usually filled with air. Under low contact pressure, the heat transfer in the gas gap is much stronger than that in the solid spot [41]. A study conducted by Lang [42] pointed out that the convective heat transfer in the gas gap is negligible when the gas gap width is less than 6 mm. In this study, the physical property parameters of air are assigned to the solid contact layer to simulate the contact thermal resistance in real situations, and the strength of the contact thermal resistance is simulated by setting different thermal conductivity coefficients. In practice, the heat transfer performance is enhanced by filling with thermal conductive adhesive. The physical parameters of the materials involved in the simulations are summarized in Table 1. In this study, the maximum temperatures of water and other solid materials are under 40°C and 100°C, respectively. Their minimum temperatures are above 25°C. In these temperature ranges, the properties of the materials used in this simulation work can be assumed as constant.

2.2. Numerical Model. The numerical simulation study of a pouch battery pack system under liquid cold plate cooling involves multiple domains and requires a multiscale coupled electrical-thermal-fluid model.

The Reynolds number (Re) of the coolant in the microchannels needs to be determined to determine the flow pattern of the fluid. It is calculated as follows:

$$\text{Re} = \frac{\rho_w u_w d_H}{\mu_w}, \quad (2)$$

where ρ_w indicates the density of water, kg/m^3; u_w indicates the velocity of water, m/s; d_H indicates the equivalent diameter of the channel, calculated according to the formula (3), m; μ_w indicates the dynamic viscosity of water, kg/(m•s).

$$d_H = \frac{4A}{S}, \quad (3)$$

where A is the cross-section area of the channel, m^2; S is the perimeter of the channel cross-section, m.

The maximum Re number involved in this study is 3000, which is in the transition zone, close to 2300; thus, it can be assumed that all flows in the calculation are laminar. In the

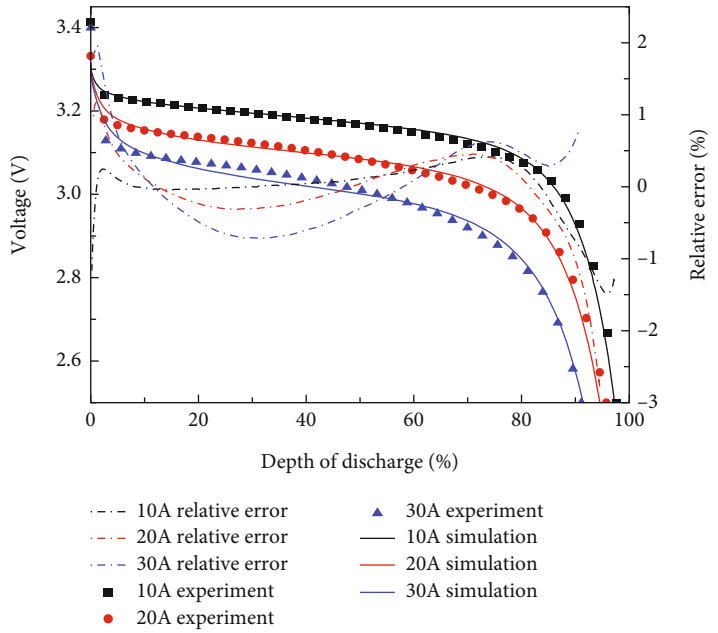

Figure 4: Comparison of the simulated I-V curves of single battery under different discharge rates with the experimental data.

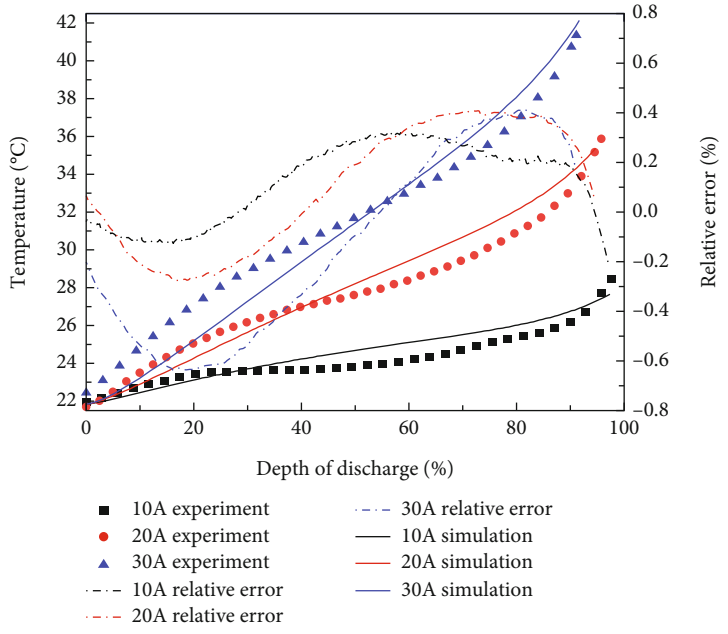

Figure 5: Comparison of the temperature evolution curves obtained from simulations for single battery under different discharge rates with experimental data.

simulation, water is assumed to be an incompressible fluid and its physical parameters do not vary with temperature. Its continuity equation is expressed as

$$\frac{\partial v_x}{\partial x} + \frac{\partial v_y}{\partial y} + \frac{\partial v_z}{\partial z} = 0, \tag{4}$$

where $\vec{v}_w$ denotes the velocity vector of the water. Its momentum equation is shown as [43]

$$\frac{\partial}{\partial t}\left(\rho_w \vec{v}_w\right) + \nabla \cdot \left(\rho_w \vec{v}_w \vec{v}_w\right) = -\nabla p + \mu_w \nabla^2 \vec{v}_w, \tag{5}$$

where p denotes the static pressure of water, Pa. Its energy equation is shown in equation (6) [44]:

$$\frac{\partial}{\partial t}\left(\rho_w C_{p,w} T_w\right) + \nabla \cdot \left(\rho_w C_{p,w} T_w \vec{v}_w\right) = \nabla \cdot \left(k_w \nabla T_w\right), \tag{6}$$

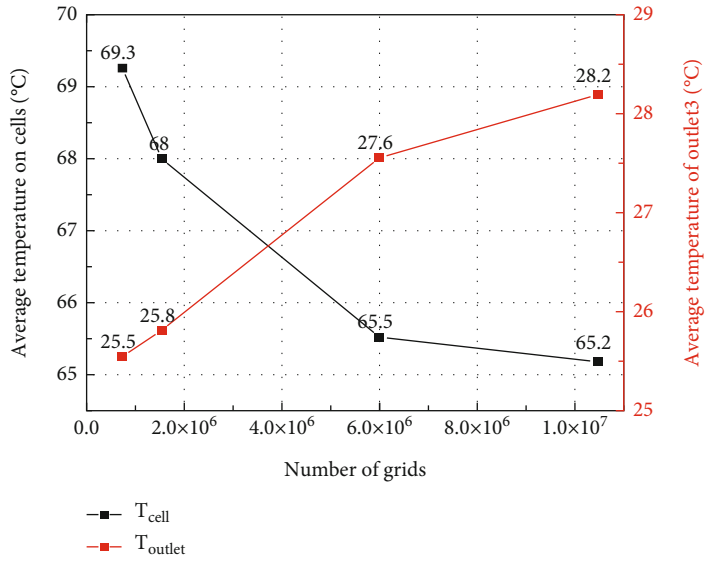

Figure 6: The average temperature on cells and the average temperature of outlet 3 of design 4 at the end of 5C discharging with 4 type meshes.

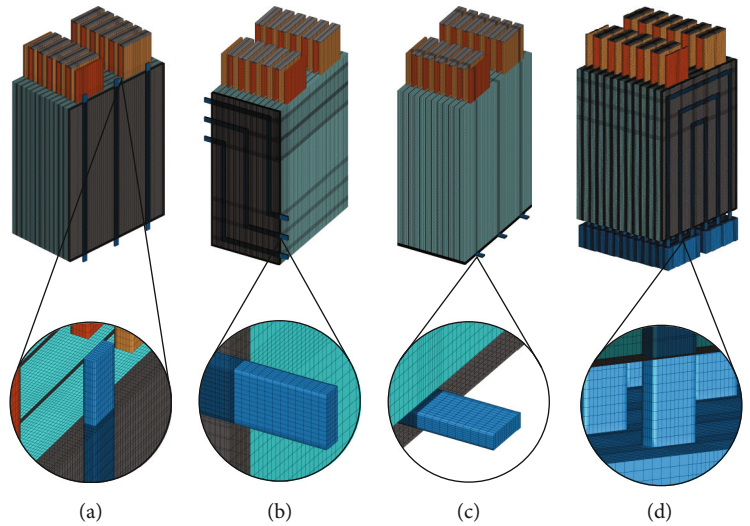

Figure 7: Meshes of the four designs: (a) design A, (b) design B, (c) design C, and (d) design D.

where $C_{p,w}$ is the specific heat capacity of water under constant pressure, J/(kg•K); k_w is the effective thermal conductivity, W/(m•K).

For the cold plate and the contact thermal resistance layer, the heat transfer process is controlled by the heat transfer differential equation:

$$\rho C_p \frac{\partial T}{\partial t} = \nabla \cdot (k \nabla T), \tag{7}$$

where ρ, C_p, and k denote the density of the corresponding material, kg/m^3, the constant pressure specific heat capacity, J/(kg•K), and the thermal conductivity, W/(m•K), respectively.

For the cell domain, the heat transfer process is controlled by [45]

$$\rho_b C_{p,b} \frac{\partial T}{\partial t} = \frac{\partial}{\partial x}\left(\lambda_x \frac{\partial T}{\partial x}\right) + \frac{\partial}{\partial y}\left(\lambda_y \frac{\partial T}{\partial y}\right) + \frac{\partial}{\partial z}\left(\lambda_z \frac{\partial T}{\partial z}\right) + \dot{Q}, \tag{8}$$

where ρ_b denotes the density of the cell domain, kg/m^3; $C_{p,b}$ denotes the constant pressure specific heat capacity of the cell, J/(kg•K); λ_x, λ_y, and λ_z denote the thermal conductivity of the cell domain in the x, y, and z directions, respectively, W/(m•K); $\dot{Q}$ denotes the heat generated by the cell during discharge, which mainly includes the heat of polarization, the heat of reaction, Joule heat, and ohmic heat [30]. It is

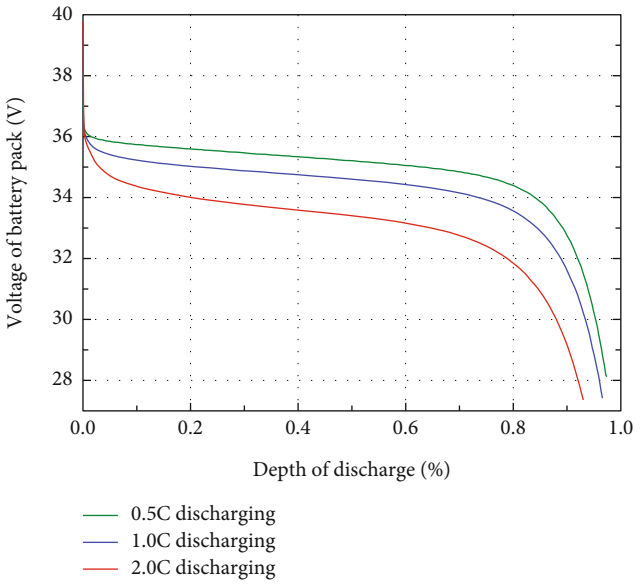

Figure 8: The voltage curves of battery pack under 0.5C, 1.0C, and 2.0C discharging conditions.

presented as the heat source of the control volume in the calculation, W/m^3.

The dual-potential multiscale multidomain (MSMD) cell model is chosen for this study to derive the temperature and electric fields of the battery, with the following set of differential equations describing the temperature distribution and potential distribution [46].

$$\frac{\partial \rho_b C_{p,b} T}{\partial t} - \nabla \cdot (\lambda \nabla T) = \sigma_+ |\nabla \phi_+|^2 + \sigma_- |\nabla \phi_-|^2 + \dot{q}_{ECh}, \quad (9)$$

$$\nabla \cdot (\sigma_+ \nabla \phi_+) = -j_{ECh}, \quad (10)$$

$$\nabla \cdot (\sigma_- \nabla \phi_-) = j_{ECh}, \quad (11)$$

where σ^+ and σ^- are the effective conductivities of the positive and negative electrodes, respectively; ϕ^+ and ϕ^- are the potentials of the positive and negative electrodes, respectively; and j_{ECh} and $\dot{q}_{ECh}$ are the volumetric current transfer density and the heat due to electrochemical reaction, respectively. Compared with equation (8), equation (9) lists the heat generated by the battery more specifically, including ohmic heat ($\sigma_+ |\nabla \phi_+|^2 + \sigma_- |\nabla \phi_-|^2$) and electrochemical heat. The volumetric current density and electrochemical heat are calculated by the subscale ECM model as follows.

$$j_{ECh} = \frac{I}{\text{Vol}}, \quad (12)$$

$$\dot{q}_{ECh} = \frac{I}{\text{Vol}} \left[V_{\text{OCV}} - (\phi_+ - \phi_-) - T \frac{\text{dU}}{\text{dT}} \right], \quad (13)$$

where I is the current; Vol denotes the volume of the cell body; V_{OCV} is the open circuit voltage. In equation (13), $I/Vol[V_{\text{OCV}} - (\phi_+ - \phi_-)]$ denotes polarization heat, and $-(I/\text{Vol})T(\text{dU/dT})$ denotes the reaction heat [47, 48]. The I-V relationship of the battery can be obtained by solving the circuit equations of the ECM model as follows:

$$\begin{aligned} V(t) &= V_{\text{OCV}}(\text{SOC}) + V_1 + V_2 - R_s(\text{SOC}) I(t), \\ \frac{\text{dV}_{\text{tran},s}}{\text{dt}} &= -\frac{1}{R_{\text{tran},s} C_{\text{tran},s}} V_{\text{tran},s} - \frac{1}{C_{\text{tran},s}} I(t), \\ \frac{\text{dV}_{\text{tran},l}}{\text{dt}} &= -\frac{1}{R_{\text{tran},l} C_{\text{tran},l}} V_{\text{tran},l} - \frac{1}{C_{\text{tran},l}} I(t), \\ \frac{d(\text{SOC})}{\text{dt}} &= \frac{I(t)}{3600 Q_{\text{ref}}}. \end{aligned} \quad (14)$$

In the above set of equations, V_{OCV}, R_{series}, $R_{\text{tran},s}$, $C_{\text{tran},s}$, $R_{\text{tran},l}$, and $C_{\text{tran},l}$ are all functions of the state of charge (SOC). The specific function relationship form was proposed by Chen and Rincon-Mora [49], in which the parameters can be obtained based on the experimental data. In this work, the I-V characteristic data of lithium-ion battery under different currents discharging and the temperature evolution data at the center of the battery outer surface are obtained experimentally. The function relationships on SOC determined from these data are shown as follows:

$$\begin{aligned} V_{\text{OCV}} &= 3.2 + 0.125\text{SOC} - 0.04\text{SOC}^2 + 0.03\text{SOC}^3 - 0.7 \exp(-18.5\text{SOC}), \\ R_{\text{series}} &= 0.015 + 0.3 \exp(-8.5\text{SOC}), \\ R_{\text{tran},s} &= 0.05 + 0.01 \exp(-29.14\text{SOC}), \\ C_{\text{tran},s} &= 703.6 - 752.9 \exp(-13.51\text{SOC}), \\ R_{\text{tran},l} &= 0.05 + 0.01 \exp(-155.2\text{SOC}), \\ C_{\text{tran},l} &= 4475 - 6056 \exp(-27.12\text{SOC}). \end{aligned} \quad (15)$$

Using the model based on these parameters, the I-V performance curves and temperature evolution curves of the single battery under different discharging rates (under constant currents of 10A, 20A, and 30A) can be well matched with the experimental data, as shown in Figures 4 and 5. The relative error of battery voltage during discharge is within 3%, and the relative error of temperature (K) is within 1%.

The inlets and outlets of designs are specified in Figure 1. All inlet boundary conditions in the research are velocity-inlet, with constant inlet velocity and inlet temperature of 25°C. All outlet boundary conditions are pressure-outlet, with atmospheric pressure at outlet. The fluid walls, as shown in Figure 2, are set as a no-slip wall boundary. All of the outer walls of the model are set as an insulation boundary. The initial temperature is 25°C. The simulations are performed on the ANSYS FLUENT platform. The spatial discretization methods of pressure, momentum, energy, and potential are second order, second order upwind, second order upwind, and first order upwind, respectively. In the simulation, the convergence criteria of velocity, energy, and potential are 10^{-6}, 10^{-9}, and 10^{-12}, respectively.

2.3. Grid Independence Analysis. The structured mesh is applied in this study for battery packs using ANSYS ICEM.

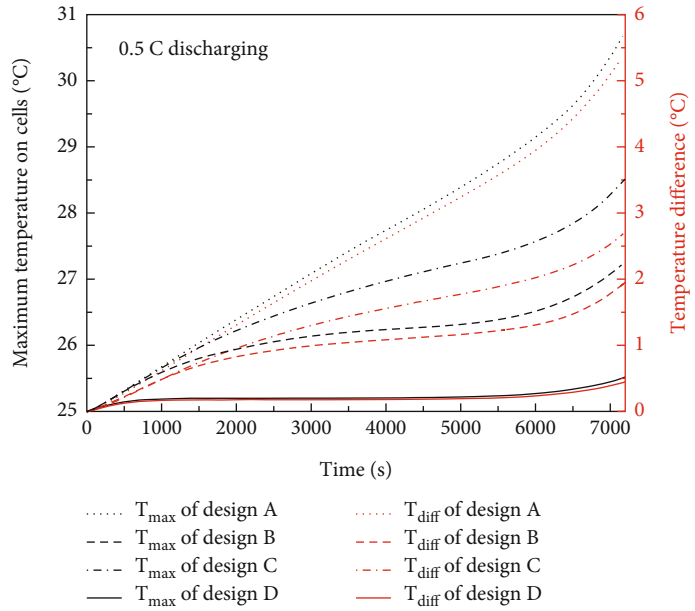

Figure 9: The maximum temperatures and maximum temperature differences on cells of four designs under 0.5C discharging.

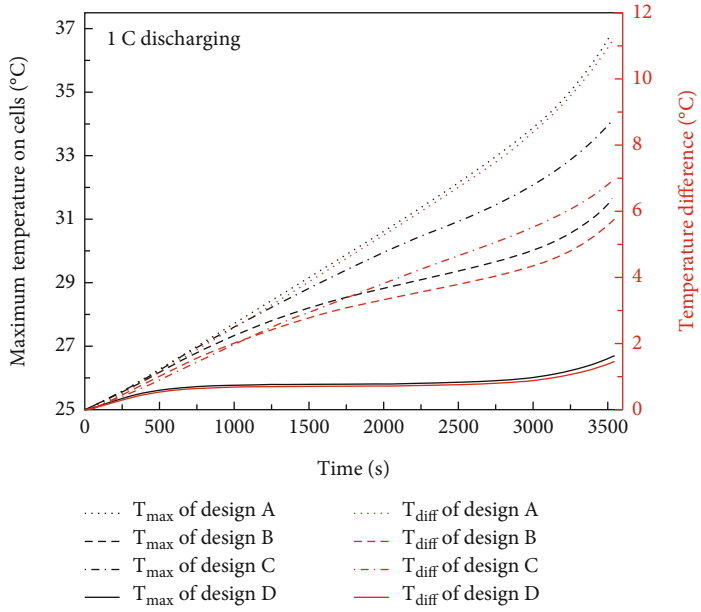

Figure 10: The maximum temperatures and maximum temperature differences on cells of four designs under 1.0C discharging.

A grid independence test was performed. Taking design C as an example, four types of meshes with numbers of 731290, 1533803, 5997744, and 10466752 were established. The average temperature on the battery pack and the surface average temperature of the third outlet on design D at the end of 5C discharging, T_{cell} and T_{oulet}, are selected for comparison in the analysis. The comparison results of different meshes are as shown in Figure 6. It is found that the mesh with 5997744 grids is already suitable for the work. A similar grid independence test was also conducted for design A, design B, and design D. The results showed that the numbers of suitable meshes for the three cases were 6173920, 7441384, and 8801884, respectively. As for the time step testing, taking the simulation result with 0.5 s time step as the reference result, the maximum temperature on battery cell is used for comparison. Modeling results of 1.0 s and 2.0 s are compared. The results shows that the deviations of maximum temperature with time testing condition of 1.0 s and 2.0 s are 0.141% and 0.460%, respectively. It is found the time step of 2.0 s is reasonable to the simulation in current work. The meshes of the four cases are shown in Figure 7.

3. Results and Discussion

3.1. The Influence of Discharging Rate on the Performance of Four Designs. This section investigates the thermal

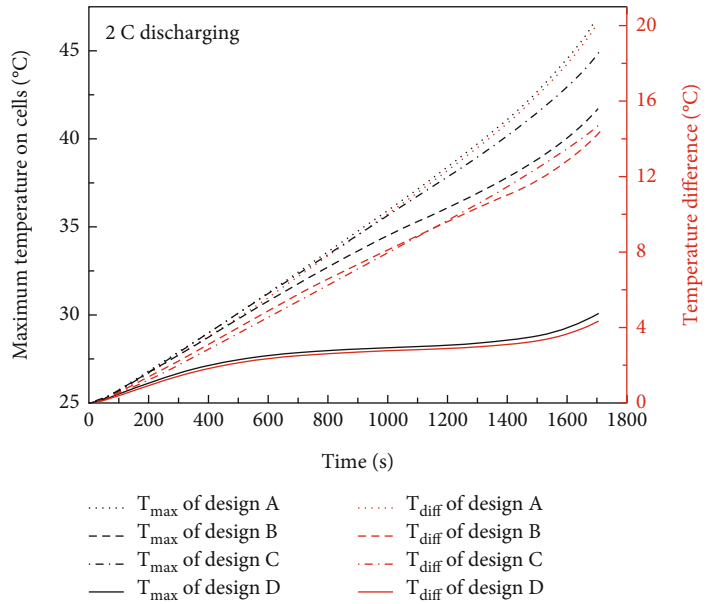

Figure 11: The maximum temperatures and maximum temperature differences on cells of four designs under 2.0C discharging.

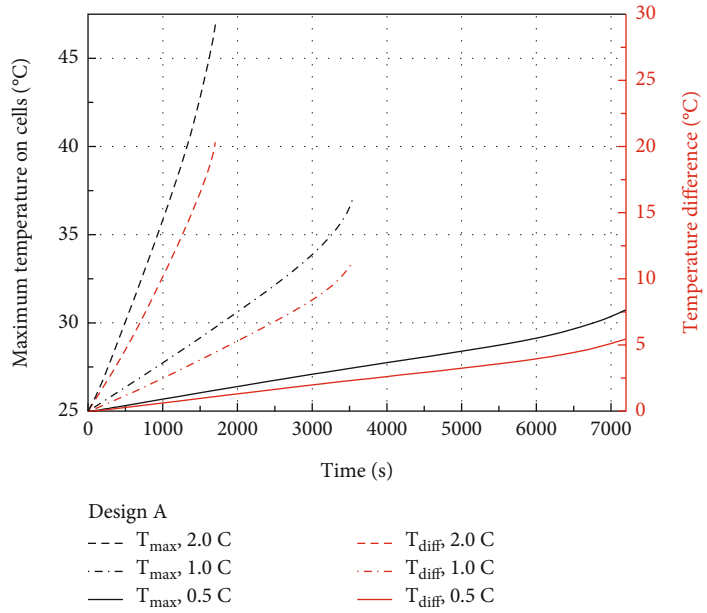

Figure 12: The maximum temperature and maximum temperature difference on cells of design A.

performance of the four designs in the discharge process at three rates of 0.5C, 1.0C, and 2.0C. The temperature rising and temperature uniformity of the four designs at different discharging rates are compared, which are reflected by the maximum temperature (T_{max}) and maximum temperature difference (T_{diff}) of the battery packs, respectively. The inlet mass flow rate of all four designs is 1.8×10^{-2} kg/s. Figure 8 depicts the I-V curves of the battery packs simulation at the three discharge rates. Due to the electrochemical characteristics of the Li-ion battery, the battery pack has a stable voltage platform in the middle of the discharge process. When discharging progress is almost finished, the lithium ions in the negative electrode will be depleted and the battery voltage drops rapidly.

Figures 9–11 show the maximum temperature and maximum temperature difference curves of the battery packs for design A, design B, design C, and design D during discharging at 0.5C, 1.0C, and 2.0C, respectively. As can be seen from the figures, the maximum temperature evolutions of the battery pack under different discharge rates show a similar pattern. The maximum temperature rises throughout the whole discharging process. The electrochemical heat is released steadily and accumulates in the middle working platform, and thus, the temperature rises steadily. At the

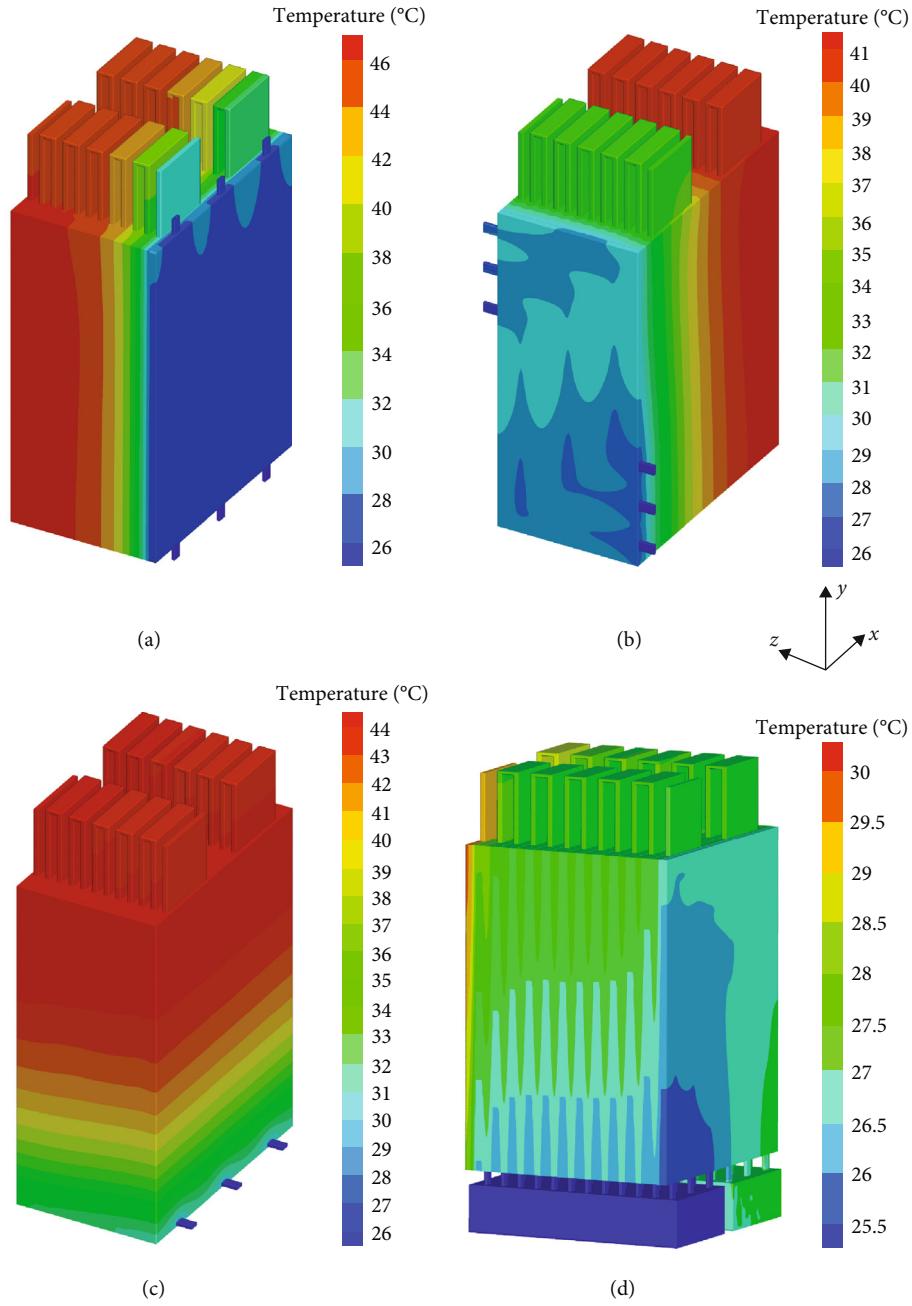

Figure 13: The temperature contours of four designs at the end of 2.0C discharging: (a) design A, (b) design B, (c) design C, and (d) design D.

Table 2: The power consumption of the pump.

Case	Design A	Design B	Design C	Design D
P (10^{-3} W)	9.32	20.5	5.52	1.18

end of the discharge, a sudden drop in voltage leads to a series generation of irreversible heat, resulting in a rapid increase in temperature. Figure 12 shows the maximum temperature and maximum temperature difference curves of design A at different discharge rates. It can be seen that the maximum temperature rises significantly, and the temperature difference increases significantly with the discharge rate accelerating. This is because the higher discharge current increases the rate of irreversible heat generation and accumulation, which further causes the increase in temperature and temperature difference [26, 50].

The maximum temperature of design A is the highest under all three discharge rates, followed by design C, design B, and finally, design D. The maximum temperature of design A is already over 30°C at 0.5C and reaches 47°C at 2.0C, which is above the optimal operating temperature range. The high-temperature zone of lithium battery degrades faster than other zones and may eventually become ineffective. Operating temperature above 40°C will accelerate the decomposition of the solid electrolyte interface (SEI) and can be detrimental to lithium-ion battery performance. The

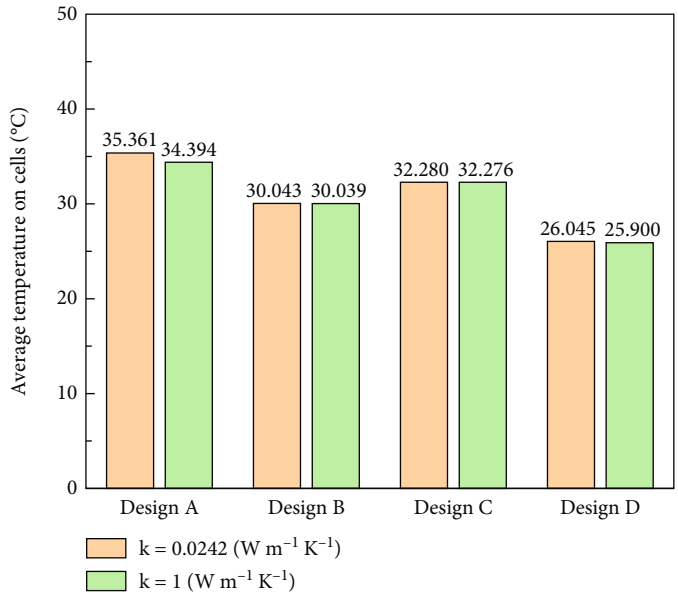

Figure 14: The average temperatures of four designs under 1.0C discharging rate with the contact layer conductivity of 0.0242 W•m^{-1}•K^{-1} and 1.0 W•m^{-1}•K^{-1}.

Table 3: The maximum temperature and the temperature difference of the battery packs.

k (W m^{-1} K^{-1})	Design A		Design B		Design C		Design D	
	T_{max} (°C)	ΔT (°C)	T_{max} (°C)	ΔT (°C)	T_{max} (°C)	ΔT (°C)	T_{max} (°C)	ΔT (°C)
0.0242	37.358	11.874	31.769	5.809	34.281	7.078	26.521	1.179
1	37.073	11.328	31.741	5.779	34.230	7.018	26.690	1.441

maximum temperature of design D is always kept within 30°C, and the entire pack is always at the optimal operating temperature. This is because compared to the other three designs design D has a stronger convection heat transfer for its high-speed coolant. In addition, increasing the discharge rate has a significant impact on design A, design B, and design C. Under 0.5C, the maximum temperature of design A, design B, and design C increased by 22.9%, 10.6%, and 16.4%, respectively, compared to the initial temperature. Under 2.0C, it increased by 88.1%, 67.5%, and 80.1%, respectively. However, the maximum temperature of design D increased by 2.1% and 20.4% under 0.5C and 2.0C, respectively, which is a small change relatively. From the perspective of temperature uniformity, the maximum temperature difference of design D is within 5°C for discharge rates. The maximum temperature differences of design A, design B, and design C increase significantly with the acceleration of discharge rate and can exceed 14°C at 2.0C, which will cause the degradation of the battery pack performance.

Figure 13 shows the temperature field of the four designs at the end of 2.0C discharging. For design A, the cells close to the cold plate are well cooled. To dissipate outside, the heat generated by the cells farther away from the cold plate needs to overcome the thermal resistance composed of multiple cells and contact layers, while the thermal conductivity of cells along the z-direction is small which means a large thermal resistance. So, the cooling effect is poor. Therefore, the temperature gradient inside each cell in design A is not obvious. The temperature difference of about 20°C in the pack comes from the temperature difference between single cells. Its highest temperature is located on the cell farthest from the cold plate. The simulation results show that at the end of discharge, the total heat productions of the nearest and farthest cells in the z-direction both are 20.09 W, while they dissipate 14.25 W and 0.14 W heat, respectively. The latter is hardly cooled. Each cell of design B is basically under the same cooling condition, so the temperature distribution of each cell is basically the same, which shows a large temperature gradient with a lower temperature zone located on the side near the cold plate. The main direction of heat transfer is the negative direction of the x-axis, and the thermal conductivity of the battery in this direction is large which means a small thermal resistance. Thus, design B has a better performance on temperature control under the same mass flow rate compared to design A. The heat dissipation direction of design C is the negative direction of the y-axis, and the thermal conductivity of the battery in this direction is the same as that in the x-axis. However, the height of the cell in the y-direction is 205.5 mm, which is larger than its length on the x-axis of 156 mm. Therefore, compared with design B, design C has a greater resistance and a slightly worse cooling performance. Design D uses 12 cold plates to achieve the fullest contact between the cold

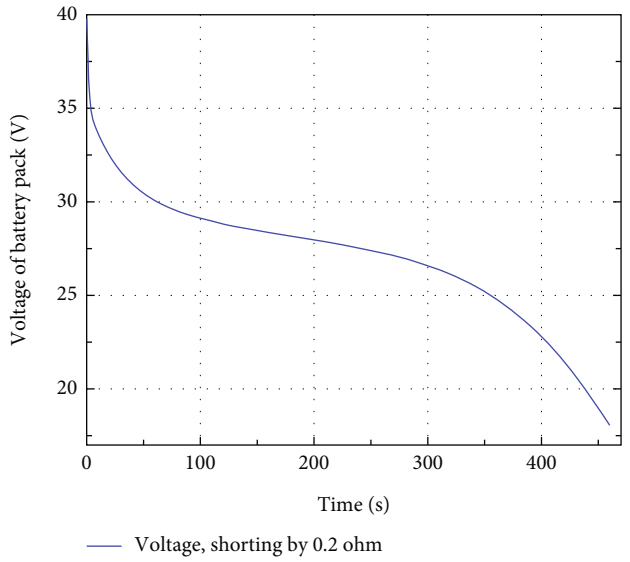

Figure 15: The battery pack voltage under 0.2 Ω external shorting condition.

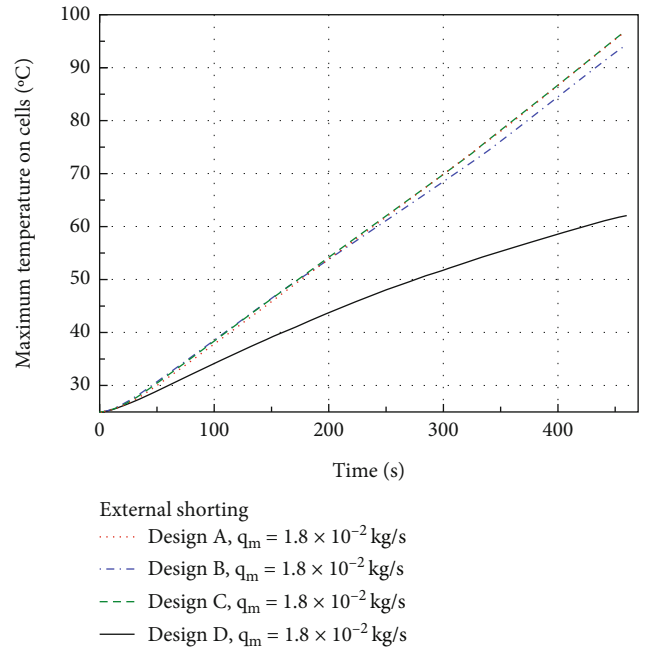

Figure 16: The maximum temperature of four designs under 0.2 Ω external shorting condition with coolant inlet mass rate of 1.8×10^{-2} kg/s.

terminal and the hot terminal, showing an excellent cooling effect, low-temperature rise, and a small temperature gradient on the pack. Compared to other cells that are between two cold plates, the farthest cell in the z-direction is only cooled by one cold plate on one side, so it shows a slightly higher temperature.

The pump power of liquid-cooled BTMS required to maintain its coolant circulation is an important parameter to evaluate its performance [51]. The power consumption of the pump is calculated as [22]

$$W = \sum_{i=1}^{n} \Delta P_i \dot{V}_i, \tag{16}$$

where i denotes the number of channels in a single system; n is the total number of channels; ΔPi denotes the pressure drop from coolant inlet to outlet, Pa; $\dot{V}_i$ denotes the volumetric flow rate of the ith channel, m^3/s. The power consumption of the four designs at the end of the discharging are reported in Table 2.

Due to the small scale of the channels, the pump power consumptions are small, and design D requires the least power consumption. Compared to design D, design A, design B, and design C need more pump power consumption, because with the same inlet mass flow, these three designs have larger inlet velocity, and thus, their pressure drops and pump power consumption are higher. In summary, design D can obtain the best cooling effect with minimum power consumption and can meet the cooling requirement of the battery pack under 0.5C, 1.0C, and 2.0C discharging conditions. In addition, it is less affected by the discharge rates, showing better stability and far better performance than other designs.

3.2. The Influence of Contact Thermal Resistance on the Performance of Four Designs. The contact thermal resistance between cells in a battery pack can have a great impact on the battery heat dissipation. Filling thermal conductive adhesive between cells can effectively reduce the temperature rise and temperature difference of the battery pack [52]. This section explores the effect of contact thermal resistance between cells on the thermal performance of four designs. The maximum temperature and the maximum temperature difference in the battery packs are used as the evaluation criteria for the thermal performance of the battery packs. The thermal conductivity of 1.0 $W \bullet m^{-1} \bullet K^{-1}$ (thermal conductivity of air) and 0.0242 $W \bullet m^{-1} \bullet K^{-1}$ (thermal conductivity of thermal adhesive) was used as the thermal conductivity of the contact thermal resistance layer in the battery pack model. The discharge rate is 1.0 C, and the coolant inlet mass flow rate is 1.8×10^{-2} kg/s.

Figure 14 shows the average temperature comparison of the four designs at the end of discharging for different thermal resistance cases. The maximum temperature and maximum temperature difference are listed in Table 3. Overall, the filling of the thermal conductive adhesive can reduce the thermal resistance during the heat transfer process, and thus, it can make a positive effect on the thermal performance of all four designs. However, the effect on design A is larger, and the effect on the others is small. In design A, the heat generated by batteries dissipate along the negative z-axis. The thermal resistance in this direction from the cold plate to the farthest cell can be calculated as

$$R_t = 12 \frac{\delta_b}{k_{b,z}} + 11 \frac{\delta_c}{k_c}, \tag{17}$$

Table 4: The maximum temperature and the temperature difference of the battery packs.

q_m (kg s^{-1})	Design A		Design B		Design C		Design D	
	T_{max} (°C)	ΔT (°C)	T_{max} (°C)	ΔT (°C)	T_{max} (°C)	ΔT (°C)	T_{max} (°C)	ΔT (°C)
3.6×10^{-3}	97.010	59.063	95.115	49.112	97.004	41.174	76.586	35.033
1.8×10^{-2}	97.010	63.042	94.531	56.921	97.123	49.088	62.081	31.532
3.6×10^{-2}	97.010	63.722	94.149	58.219	96.894	50.689	55.530	26.837

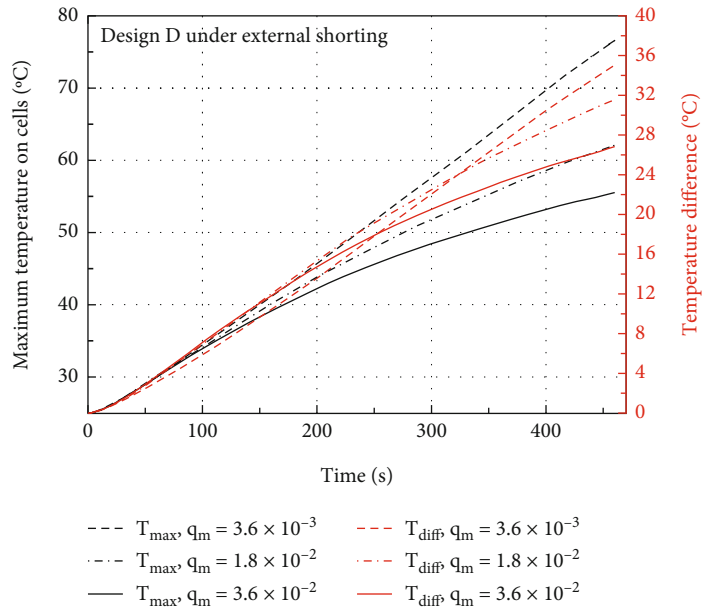

Figure 17: The maximum temperature and temperature difference of design D under 0.2 Ω external shorting condition with coolant inlet mass rate of 3.6×10^{-3} kg/s, 1.8×10^{-2} kg/s, and 3.6×10^{-2} kg/s.

where δ_b and δ_c are the thicknesses of cell and contact layer, m, respectively; $k_{b,z}$ and k_c are the thermal conductivity of cell and contact layer in z-direction, W•m^{-1}•K^{-1}, respectively. When the thermal conductivity of contact thermal layer is 1.0 W•m^{-1}•K^{-1} and 0.0242 W•m^{-1}•K^{-1}, the thermal resistances from the cold plate to the farthest cell are 0.361 m^2•K/W and 0.094 m^2•K/W, respectively. 74% of the thermal resistance is reduced by filling with thermal conductive adhesive. For design B and design C, the thermal resistances are not significantly weakened. The average temperature, maximum temperature, and temperature difference are all slightly reduced. For design D, the filling of the thermally conductive adhesive improves the heat transfer between the cold plate and the cells, but the maximum temperature and temperature difference increase instead. This is because in design D, for the cell farthest from the cold plate, only one side is cooled, and the cold plate attached to it not only cools it but also provides cooling to its neighboring cell. The increased thermal conductivity of the contact layer enhances the cooling of the adjacent cell by the cold plate and also leads to a slight weakening of its ability to cool the farthest cell. At the end of discharging, the total heat dissipated through the cold plate by the farthest cell with contact layer $k = 0.0242$ W•m^{-1}•K^{-1} is 4.955 W, while this value is 4.793 W for contact layer $k = 1.0$ W•m^{-1}•K^{-1}. The addition of the thermal conductive adhesive improves the heat dissipation of the BTMS, with different magnitudes of enhancement for different designs. However, the reduction in contact thermal resistance does not necessarily improve the thermal performance of the system, depending on the situation. Design D shows a small decrease in thermal performance with the increase of contact layerss thermal conductivity, but its performance is still superior.

3.3. The Performances of Four Designs under External Short Circuit Condition. Under external short circuit condition, the battery pack will discharge at a high current in a very short time and cause a rapid temperature rise, which may trigger thermal runaway, combustion, and explosion. A suitable thermal management design can effectively limit the temperature rise and temperature gradient of the battery pack under external short circuit condition [29] and also prevent the further spread of thermal runaway in the battery pack when it occurs [53]. In this section, the performance of four designs under 0.2 Ω external short circuit condition is explored, and further, studies on the effect of coolant inlet flow rate on thermal performance are carried out.

The voltage response of the battery pack under 0.2 Ω external short circuit condition is shown in Figure 15. Figure 16 depicts the temperature response of the four

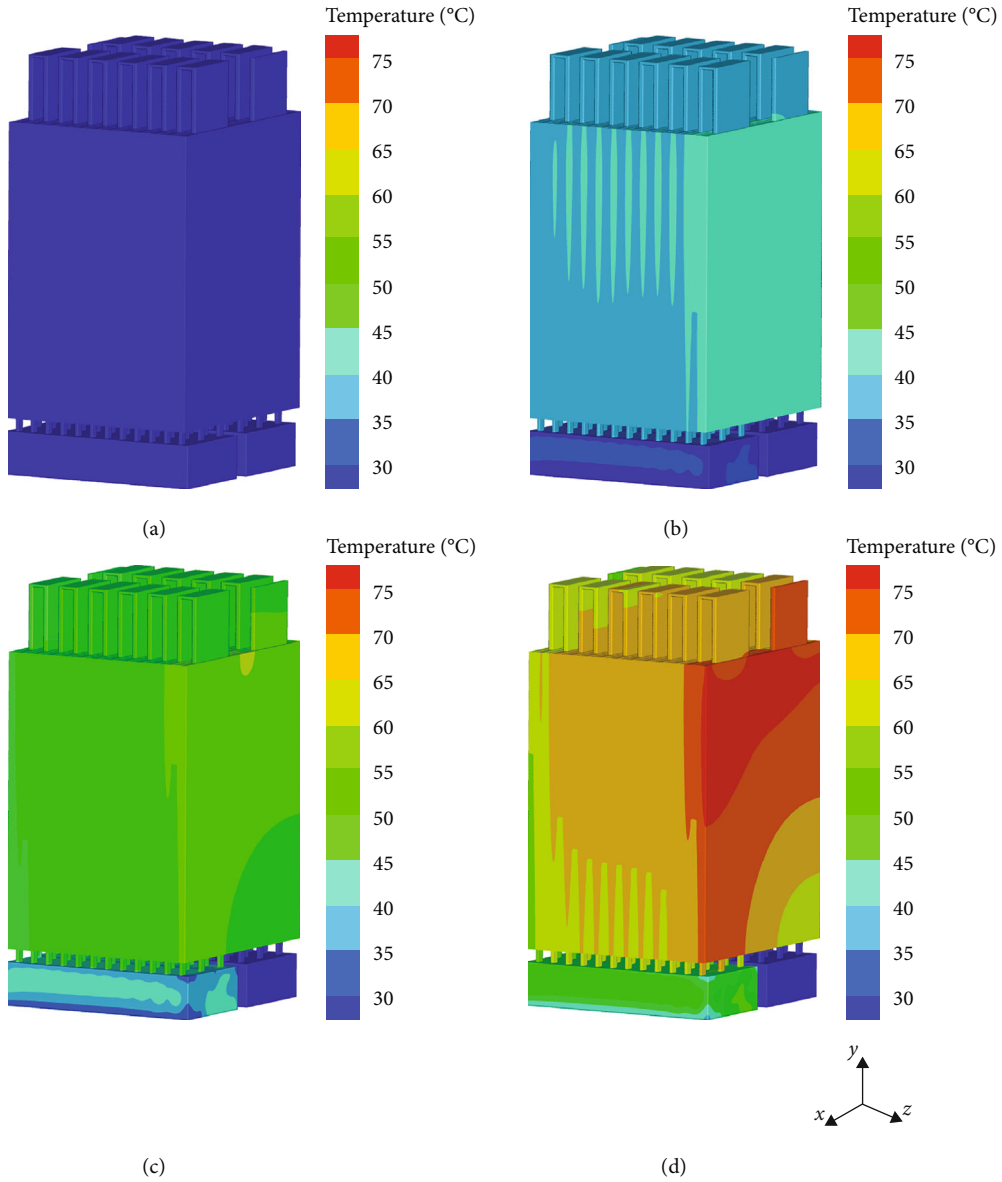

Figure 18: The temperature contour evolution of design D under 0.2 Ω external shorting condition with coolant inlet mass rate of 3.6×10^{-3} kg/s at (a) 115 s, (b) 230 s, (c) 345 s, and (d) 460 s.

designs. The battery pack discharges within 460 s, and the temperature rises rapidly. The maximum temperatures of design A, design B, and design C easily exceeds 80°C which means the battery pack is in danger of thermal runaway. Design D has a lower maximum temperature of about 60°C due to its excellent cooling performance, but still exhibits a significant temperature rise. Under external short circuit condition, the current of the pack during discharging process is so high that batteries generate a large heat, and thus, the significant increase in temperature occurs on the pack.

The maximum temperature and temperature difference of the four designs with inlet flow rates of 3.6×10^{-3} kg/s, 1.8×10^{-2} kg/s, and 3.6×10^{-2} kg/s under 0.2 Ω external short circuit condition are shown in Table 4. For design A, design B, and design C, the increase in coolant flow rate does not significantly enhance the cooling effect but worsens the uniformity of temperature distribution on the battery pack. In addition, the maximum temperature and temperature difference of all three show a tendency to approach a constant value with the increase of the mass flow rate. It indicates that increasing the coolant mass flow rate has a limited and weak effect on the thermal performance of design A, design B, and design C.

In contrast, the maximum temperature and temperature difference of design D decrease steadily with the increase of the coolant mass flow rate. Figure 17 plots the maximum temperature and temperature difference of design D for the three mass flow rates under 0.2 Ω external short circuit condition. With low flow mass rates, design D still has the possibility to exceed the 80°C temperature. The increase in mass flow rate significantly enhances its cooling capability,

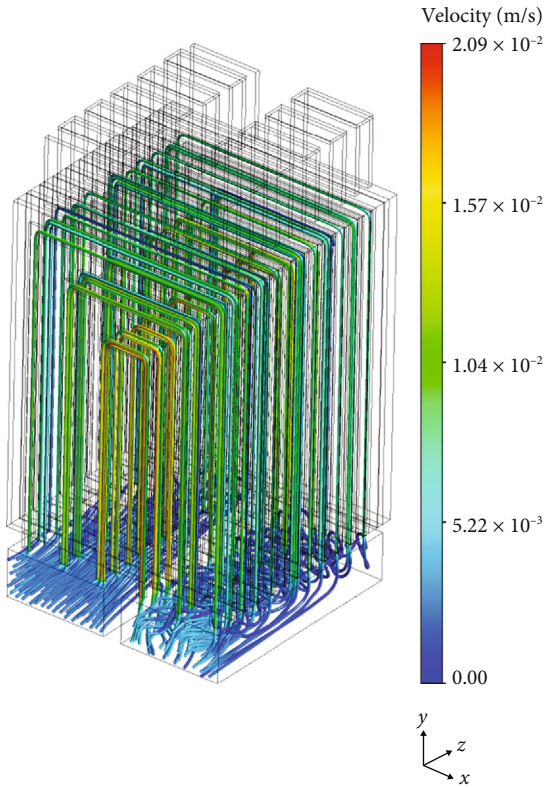

Figure 19: Velocity streamlines for design D with coolant mass flow rate of 3.6 × 10 − 3 kg/s.

reducing the maximum temperature by 27.5% and the temperature difference by 23.4%, avoiding the risk of thermal runaway and mitigating the capacity degradation and performance deterioration caused by uneven temperature under external short circuit condition. In addition, it can be predicted from the curve trend in the figure that when the coolant mass flow rate is 3.6 × 10 − 2 kg/s, and there is still potential to continue to enhance the cooling effect by increasing the mass flow rate.

Figure 18 shows the temperature contour evolution of design D at 115 s, 230 s, 345 s, and 460 s with a coolant mass flow rate of 3.6×10^{-3} kg/s under external short circuit condition. The pack temperature rises rapidly in a short period time, and multiple cells show a high-temperature about 70°C at the end of discharge. The highest temperature is still located on the farthest cell on the z-axis and is biased towards the positive direction of the x-axis due to its proximity to the outlet, where the coolant temperature is higher and the heat transfer ability is lower. It can be speculated that if another cold plate is attached to the outer side of the farthest cell, the cooling performance of the whole battery pack will be further improved. Figure 19 shows the flow field of design D with a coolant mass flow rate of 3.6 × 10 − 3 kg/s under external short circuit condition. It is observed that the coolant in design D is uniformly distributed among the cells with a high velocity, which enables efficient heat transfer so that design D shows better performance and can control the temperature below 80°C under extreme external short circuit condition with the same mass flow rate.

4. Conclusions

In this study, four designs of battery thermal management based on the microfluidic liquid cold plate are proposed for a 35 V battery pack composed of 12 $LiFePO_4$ pouch batteries connected in series. The corresponding three-dimensional electrical-thermal-fluid model is established, based on which numerical studies are conducted to explore and compare the cooling effects of the four designs in terms of discharge rate, contact thermal resistance, and external short circuit condition. The simulation results show that:

(a) Design D shows superior performance under three discharge rates of 0.5C, 1.0C, and 2.0C, and it achieves the best cooling effect with the lowest pump power consumption

(b) The reduction of contact thermal resistance between cells or between cells and cold plates in the battery pack has a different effect on cold plate thermal management system with different arrangements. With the reduction of contact thermal resistance, the heat dissipation of cold plates increases. However, in general, the reduction of contact thermal resistance has a negligible effect on these four thermal management systems

(c) Increasing the inlet mass rate can enhance the heat dissipation capability of BTMS, but the magnitude of enhancement varies for different arrangements. As for design A, design B, and design C, increasing their coolant mass flow rate has a very weak effect on the thermal performance enhancement. However, increasing the mass flow rate can reduce the maximum temperature and the temperature difference of design D apparently, keeping the battery pack under a safe working condition

Design D is slightly complex, but with excellent cooling, minimal power consumption, and the ability to handle extreme conditions such as external short circuits, it is an excellent method for battery thermal management. In addition, it can be further optimized (for example, adding a cold plate after the last cell so that each cell is cooled by two cold plates) to achieve better thermal performance.

Most existing studies on microchannel cold plates have focused on optimizing the structure, number, flow direction, and flow rate of the flow channels. There has been little discussion on the arrangement of the cold plate. This study investigates the thermal effect of different minichannel cold plate arrangements. However, this work conducted only in numerical simulation method without experimental demonstration. It needs further experimental research. This work can provide a reference for the selection and design of BTMS.

Data Availability

No underlying data was collected or produced in this study.

Conflicts of Interest

The authors declare that they have no conflicts of interest.

Acknowledgments

This work is supported by the National Natural Science Foundation of China (Grant nos. 52106226, 51876027, and 52176058) and the Fundamental Research Funds for the Central Universities, China (DUT20RC(3)095 and DUT20JC21).

References

[1] T. Pavlović, D. Mirjanić, I. R. Mitić, and A. M. Stanković, "The Impact of Electric Cars Use on the Environment," in *New Technologies, Development and Application II. NT 2019. Lecture Notes in Networks and Systems, vol 76*, I. Karabegović, Ed., Springer, Cham, 2020.

[2] J. M. Tarascon and M. Armand, "Issues and challenges facing rechargeable lithium batteries," *Nature*, vol. 414, no. 6861, pp. 359–367, 2001.

[3] X. Li, Z. Wang, and L. Zhang, "Co-estimation of capacity and state-of-charge for lithium-ion batteries in electric vehicles," *Energy*, vol. 174, pp. 33–44, 2019.

[4] M. S. Akhtar, P. T. M. Bui, Z.-Y. Li et al., "Impact of porous Mn3O4 nanostructures on the performance of rechargeable lithium ion battery: excellent capacity and cyclability," *Solid State Ionics*, vol. 336, pp. 31–38, 2019.

[5] N. Takami, K. Ise, Y. Harada, T. Iwasaki, T. Kishi, and K. Hoshina, "High-energy, fast-charging, long-life lithium-ion batteries using TiNb2O7 anodes for automotive applications," *Journal of Power Sources*, vol. 396, pp. 429–436, 2018.

[6] W. H. Zhu, Y. Zhu, and B. J. Tatarchuk, "Self-discharge characteristics and performance degradation of Ni-MH batteries for storage applications," *International Journal of Hydrogen Energy*, vol. 39, no. 34, pp. 19789–19798, 2014.

[7] S. M. A. S. Bukhari, J. Maqsood, M. Q. Baig, S. Ashraf, and T. A. Khan, "Comparison of characteristics-lead acid, nickel based, lead crystal and lithium based batteries," in *2015 17th UKSim-AMSS International Conference on Modelling and Simulation (UKSim)*, pp. 444–450, Cambridge, UK, 2015.

[8] A. Pesaran, S. Santhanagopalan, and G. Kim, *Addressing the impact of temperature extremes on large format li-ion batteries for vehicle applications (presentation)*, National Renewable Energy Lab.(NREL), Golden, CO (United States), 2013.

[9] A. Väyrynen and J. Salminen, "Lithium ion battery production," *The Journal of Chemical Thermodynamics*, vol. 46, pp. 80–85, 2012.

[10] S. Ma, M. Jiang, P. Tao et al., "Temperature effect and thermal impact in lithium-ion batteries: a review," *Progress in Natural Science: Materials International*, vol. 28, no. 6, pp. 653–666, 2018.

[11] A. M. Aris and B. Shabani, "An experimental study of a lithium ion cell operation at low temperature conditions," *Energy Procedia*, vol. 110, pp. 128–135, 2017.

[12] Y. Zhang, H. Ge, J. Huang, Z. Li, and J. Zhang, "A comparative degradation study of commercial lithium-ion cells under low-temperature cycling," *RSC Advances*, vol. 7, no. 37, pp. 23157–23163, 2017.

[13] M.-T. F. Rodrigues, G. Babu, H. Gullapalli et al., "A materials perspective on Li-ion batteries at extreme temperatures," *Nature Energy*, vol. 2, no. 8, 2017.

[14] H. Gabrisch, Y. Ozawa, and R. Yazami, "Crystal structure studies of thermally aged LiCoO2 and LiMn2O4 cathodes," *Electrochimica Acta*, vol. 52, no. 4, pp. 1499–1506, 2006.

[15] T. M. Bandhauer, S. Garimella, and T. F. Fuller, "A critical review of thermal issues in lithium-ion batteries," *Journal of the Electrochemical Society*, vol. 158, no. 3, p. R1, 2011.

[16] R. M. Spotnitz, J. Weaver, G. Yeduvaka, D. H. Doughty, and E. P. Roth, "Simulation of abuse tolerance of lithium-ion battery packs," *Journal of Power Sources*, vol. 163, no. 2, pp. 1080–1086, 2007.

[17] G. L. Woods, K. L. White, D. K. Vanderwall et al., "A mule cloned from fetal cells by nuclear transfer," *Science*, vol. 301, no. 5636, p. 1063, 2003.

[18] J. Sun, J. Li, T. Zhou et al., "Toxicity, a serious concern of thermal runaway from commercial Li-ion battery," *Nano Energy*, vol. 27, pp. 313–319, 2016.

[19] R. Mahamud and C. Park, "Reciprocating air flow for Li-ion battery thermal management to improve temperature uniformity," *Journal of Power Sources*, vol. 196, no. 13, pp. 5685–5696, 2011.

[20] A. A. Pesaran, "Battery thermal models for hybrid vehicle simulations," *Journal of Power Sources*, vol. 110, no. 2, pp. 377–382, 2002.

[21] W. Wu, S. Wang, W. Wu, K. Chen, S. Hong, and Y. Lai, "A critical review of battery thermal performance and liquid based battery thermal management," *Energy Conversion and Management*, vol. 182, pp. 262–281, 2019.

[22] D. Chen, J. Jiang, G.-H. Kim, C. Yang, and A. Pesaran, "Comparison of different cooling methods for lithium ion battery cells," *Applied Thermal Engineering*, vol. 94, pp. 846–854, 2016.

[23] J. Wang, S. Lu, Y. Wang, C. Li, and K. Wang, "Effect analysis on thermal behavior enhancement of lithium-ion battery pack with different cooling structures," *Journal of Energy Storage*, vol. 32, article 101800, 2020.

[24] W. Zichen and D. Changqing, "A comprehensive review on thermal management systems for power lithium-ion batteries," *Renewable and Sustainable Energy Reviews*, vol. 139, article 110685, 2021.

[25] Z. Qian, Y. Li, and Z. Rao, "Thermal performance of lithium-ion battery thermal management system by using mini-channel cooling," *Energy Conversion and Management*, vol. 126, pp. 622–631, 2016.

[26] C. Zhao, W. Cao, T. Dong, and F. Jiang, "Thermal behavior study of discharging/charging cylindrical lithium-ion battery module cooled by channeled liquid flow," *International Journal of Heat and Mass Transfer*, vol. 120, pp. 751–762, 2018.

[27] W. Zhang, Z. Liang, X. Yin, and G. Ling, "Avoiding thermal runaway propagation of lithium-ion battery modules by using hybrid phase change material and liquid cooling," *Applied Thermal Engineering*, vol. 184, article 116380, 2021.

[28] A. Abaza, S. Ferrari, H. K. Wong et al., "Experimental study of internal and external short circuits of commercial automotive pouch lithium-ion cells," *Journal of Energy Storage*, vol. 16, pp. 211–217, 2018.

[29] Y. Li, Z. Zhou, and W.-T. Wu, "Three-dimensional thermal modeling of Li-ion battery cell and 50 V Li-ion battery pack cooled by mini-channel cold plate," *Applied Thermal Engineering*, vol. 147, pp. 829–840, 2019.

[30] H. Liu, Z. Wei, W. He, and J. Zhao, "Thermal issues about Li-ion batteries and recent progress in battery thermal management systems: a review," *Energy Conversion and Management*, vol. 150, pp. 304–330, 2017.

[31] Z. Shang, H. Qi, X. Liu, C. Ouyang, and Y. Wang, "Structural optimization of lithium-ion battery for improving thermal performance based on a liquid cooling system," *International Journal of Heat and Mass Transfer*, vol. 130, pp. 33–41, 2019.

[32] L. Song, H. Zhang, and C. Yang, "Thermal analysis of conjugated cooling configurations using phase change material and liquid cooling techniques for a battery module," *International Journal of Heat and Mass Transfer*, vol. 133, pp. 827–841, 2019.

[33] T. F. Fuller, M. Doyle, and J. Newman, "Simulation and optimization of the dual lithium ion insertion cell," *Journal of the Electrochemical Society*, vol. 141, pp. 1–10, 1994.

[34] M. Doyle, T. F. Fuller, and J. Newman, "Modeling of galvanostatic charge and discharge of the lithium/polymer/insertion cell," *Journal of the Electrochemical Society*, vol. 140, pp. 1526–1533, 2019.

[35] B. Yannliaw, "Modeling of lithium ion cells–A simple equivalent-circuit model approach," *Solid State Ionics*, vol. 175, no. 1-4, pp. 835–839, 2004.

[36] S. M. Mousavi and G. M. Nikdel, "Various battery models for various simulation studies and applications," *Renewable and Sustainable Energy Reviews*, vol. 32, pp. 477–485, 2014.

[37] H. Zhang and M.-Y. Chow, "Comprehensive dynamic battery modeling for PHEV applications," in *IEEE PES General Meeting*, Minneapolis, MN, USA, July 2010.

[38] Y. Liu and J. Zhang, "Design a *J*-type air-based battery thermal management system through surrogate-based optimization," *Applied Energy*, vol. 252, article 113426, 2019.

[39] Q.-K. Wang, Y.-J. He, J.-N. Shen, Z.-F. Ma, and G.-B. Zhong, "A unified modeling framework for lithium-ion batteries: an artificial neural network based thermal coupled equivalent circuit model approach," *Energy*, vol. 138, pp. 118–132, 2017.

[40] P. Taheri and M. Bahrami, "Temperature rise in prismatic polymer lithium-ion batteries: an analytic approach," *SAE International Journal of Passenger Cars - Electronic and Electrical Systems*, vol. 5, no. 1, pp. 164–176, 2012.

[41] C. Madhusudana, "Thermal contact conductance and rectification at low joint pressures," *International Communications in Heat and Mass Transfer*, vol. 20, no. 1, pp. 123–132, 1993.

[42] P. M. Lang, "Calculating heat transfer across small gas-filled gaps," *Nucleonics (US) Ceased Publication*, vol. 20, 1962.

[43] G. K. Batchelor, *An introduction to fluid dynamics*, Cambridge University Press, 2000.

[44] A. Bejan, *Convection heat transfer*, John Wiley & Sons, 2013.

[45] S. C. Chen, C. C. Wan, and Y. Y. Wang, "Thermal analysis of lithium-ion batteries," *Journal of Power Sources*, vol. 140, no. 1, pp. 111–124, 2005.

[46] A. Fluent, *Advanced Add-On Modules Manual ANSYS®*, SAS IP Inc, Inc Canonsburg, PA, 2015.

[47] W. Gu and C. Wang, "Thermal-electrochemical modeling of battery systems," *Journal of the Electrochemical Society*, vol. 147, no. 8, p. 2910, 2000.

[48] D. Bernardi, E. Pawlikowski, and J. Newman, "A general energy balance for battery systems," *Journal of the Electrochemical Society*, vol. 132, no. 1, pp. 5–12, 1985.

[49] M. Chen and G. A. Rincon-Mora, "Accurate electrical battery model capable of predicting runtime and I-V performance," *IEEE Transactions on Energy Conversion*, vol. 21, no. 2, pp. 504–511, 2006.

[50] Y. Reynier, R. Yazami, and B. Fultz, "Thermodynamics of lithium intercalation into graphites and disordered carbons," *Journal of the Electrochemical Society*, vol. 151, no. 3, p. A422, 2004.

[51] M. Akbarzadeh, J. Jaguemont, T. Kalogiannis et al., "A novel liquid cooling plate concept for thermal management of lithium-ion batteries in electric vehicles," *Energy Conversion and Management*, vol. 231, article 113862, 2021.

[52] X. Xu, F. Jiang, J. Tian, R. Li, and J. Fu, "A research on the heat flow field characteristics of battery pack based on heat conduction glue cooling," *Automotive and Energy*, vol. 39, pp. 889–894, 2017.

[53] R. Zhao, J. Liu, and J. Gu, "Simulation and experimental study on lithium ion battery short circuit," *Applied Energy*, vol. 173, pp. 29–39, 2016.